ML-reconstruction for TOF-PET with Simultaneous Estimation of the Attenuation Factors

Ahmadreza Rezaei*, Michel Defrise, and Johan Nuyts

***Abstract*—In positron emission tomography (PET), attenuation correction is typically done based on information obtained from transmission tomography. Recent studies show that time-of-flight (TOF) PET emission data allow joint estimation of activity and attenuation images. Mathematical analysis revealed that the joint estimation problem is determined up to a scale factor. In this work, we propose a maximum likelihood reconstruction algorithm that jointly estimates the activity image together with the sinogram of the attenuation factors. The algorithm is evaluated with 2D and 3D simulations as well as clinical TOF-PET measurements of a patient scan and compared to reference reconstructions. The robustness of the algorithm to possible imperfect scanner calibration is demonstrated with reconstructions of the patient scan ignoring the varying detector sensitivities.**

***Index Terms*—joint activity and attenuation estimation, maximum likelihood, self-normalization, time-of-flight (TOF) positron emission tomography (PET)**

I. INTRODUCTION

A quantitative reconstruction of the tracer activity distribution in positron emission tomography (PET) requires correction of the emission data for the attenuation factors. In current PET/CT systems, attenuation correction is typically done by means of well-aligned CT images adjusted to the photon energy of 511 keV [1], [2]. However, because the PET and CT scans are acquired sequentially and because the acquisition durations are very different, the images are not perfectly matched, and PET attenuation correction artifacts are unavoidable [3]. These inaccurate tracer distribution values are the result of respiratory and/or patient motion during and between the two scans. Several research groups have tried to estimate the activity and attenuation images simultaneously from non time-of-flight (TOF) PET emission data, in an attempt to overcome this problem [4]–[12]. Despite some useful results the problem of joint estimation was found to be highly ill-posed. However, recent studies show that the data redundancy in TOF-PET data allows stable reconstruction of both attenuation and activity from TOF-PET emission data [13]–[15]. Moreover, mathematical analysis revealed that the TOF-PET data determine the attenuation correction factors uniquely except for a scale factor [16].

As well as correction for the attenuation factors, the PET data need to be corrected for the sensitivity differences between different lines-of-response (LORs). Commonly, these detector pair sensitivities are estimated by means of dedicated calibration scans, where the response of each LOR is measured for known activity phantoms [17], [18]. However, the detector pair sensitivities are prone to change from one scan to the other, thus potentially resulting in sub-optimal tracer distribution reconstructions [19]. In an attempt to overcome this issue, some researchers have proposed to jointly estimate tracer activity distributions together with detector pair sensitivities [20], [21]. These “self-normalizing” algorithms make an attempt to refine the PET detector pair sensitivities which were originally obtained from previous calibration scans.

In this paper, we propose a new maximum likelihood algorithm (called MLACF) that jointly estimates the image of the activity distribution and the sinogram with the attenuation factors. We also show that the algorithm is robust to errors in the detector pair sensitivities. This method avoids the reconstruction of the attenuation image, and thus requires some a-priori knowledge about the activity or the attenuation factors to be quantitatively accurate. In its most general form, the algorithm must keep an image of the tracer distribution and a sinogram of the attenuation factors in memory during reconstruction. However, if additive contributions (such as scatter and/or randoms) can be ignored, the algorithm does not even require the storage of the attenuation correction factors. It has been shown in the latter case that when the emission data are consistent, the log-likelihood can be expressed in a “reduced” form and that the solution space to this reduced log-likelihood is free of possible local maxima [15], [22]. Further properties and some convergence analysis of the scatter and randoms free case can be found in [22], [23].

The paper is organized as follows: in section II the algorithm is derived and a theoretical analysis of its convergence is given. Section III describes 2D and 3D simulations so as to compare activity reconstructions of the newly proposed method to reference activity reconstructions of the well established MLEM and the MLAA (maximum likelihood activity and attenuation reconstruction [7], [14]) methods. The new algorithm does not impose the consistency of the attenuation sinogram, i.e. the estimated attenuation sinogram will not in general be equal to the projection of a non-negative attenuation image. Since this may result in increased noise, we analyze its noise properties in 2D simulations. The results of these simulations are shown and compared, together with results of a patient scans in section IV. We conclude the paper by discussing the results and drawing some conclusions in section V.

Manuscript received ...; revised ...; accepted .... Date of publication ...; date of current version .... This research is supported by a research grant (GOA/11/006) from K.U. Leuven, FWO project G027514N and by Siemens Healthcare. *Asterisk indicates corresponding author.*

A. Rezaei and J. Nuyts are with the Nuclear Medicine Department, K.U. Leuven, B-3000, Leuven, Belgium, (e-mails: ahmadreza.rezaei@uz.kuleuven.be, johan.nuyts@uz.kuleuven.be)

M. Defrise is with the Nuclear Medicine Department, Vrije Universiteit Brussel, B-1090 Brussels, Belgium. (e-mail: mdefrise@vub.ac.be)

Digital Object Identifier ...

II. METHODS

A. MLACF

In TOF-PET, the expected count $\bar{y}_{it}$ for line-of-response (LOR) i and TOF-bin t can be expressed as

$$\bar{y}_{it} = a_i p_{it} + s_{it} \tag{1}$$

for,

$$a_i = e^{-\sum_{j=1}^{J} l_{ij}\mu_j}, \quad p_{it} = \sum_{j=1}^{J} c_{ijt}\lambda_j$$

where a_i is the attenuation factor of LOR i, p_{it} is the (unattenuated) TOF projection of the activity image for LOR i and TOF-bin t and s_{it} is the expected additive contribution of scatter and/or randoms. λ_j and μ_j are the activity and attenuation coefficient at voxel j, c_{ijt} is the sensitivity of the measurement bin at (i, t) for activity in j in absence of attenuation and l_{ij} is the effective intersection length of LOR i with voxel j. We represent summation over the TOF-index (corresponding to the non-TOF values) by dropping the t index, e.g. $c_{ij} = \sum_t c_{ijt}$. The same convention is also used for the non-TOF measurements y_i and p_i.

The Poisson log-likelihood function for the emission measurements y_{it} is then expressed as

$$L(y, \lambda, a) = \sum_{it} y_{it} \log \bar{y}_{it}(\lambda, a) - \bar{y}_{it}(\lambda, a) \tag{2}$$

where we wish to estimate λ and a by maximizing (2). We propose an alternated optimization approach: first a is updated keeping λ fixed, and then λ is updated keeping a fixed. The monotonic iterative algorithm (referred to below as MLACF) which preserves the non-negativity of all variables is given by:

$$\begin{aligned} a_i^{k+1} &= a_i^k + \frac{a_i^k}{p_i^h} \left. \frac{\partial L(y, \lambda^h, a)}{\partial a_i} \right|_{a^k} \\ &= a_i^k \sum_t \frac{p_{it}^h}{p_i^h} \frac{y_{it}}{a_i^k p_{it}^h + s_{it}} \end{aligned} \tag{3}$$

$$\lambda_j^{h+1} = \frac{\lambda_j^h}{\sum_i c_{ij} a_i^{k+1}} \sum_{it} c_{ijt} a_i^{k+1} \frac{y_{it}}{\sum_\xi c_{i\xi t} a_i^{k+1} \lambda_\xi^h + s_{it}} \tag{4}$$

where the superscripts h and k represent the iteration, and the algorithm is initialized with $a_i^0 > 0$ and $\lambda_j^0 > 0$. We used two iteration symbols, because the optimization could be done by alternately applying a few updates (3) followed by a few updates of (4). An ordered subsets version of the MLACF algorithm is obtained in the standard way, i.e. by restricting the summations over i in (4) to the LORs in the subset.

B. Convergence

The second step (4) is the standard TOF-MLEM algorithm, which is known to monotonically increase the likelihood [24]. In the following, we show that the first step (3) iteratively increases the likelihood as well. Moreover, we show that at fixed $\lambda = \lambda^h$ (the superscripts of the activity estimate and its corresponding (non-) TOF projection will be dropped for convenience), with repeated application of (3) the attenuation factor estimate a converges to the constrained maximizer

$$a^* = \arg\max_{a \geq 0} L(y, \lambda, a) \tag{5}$$

The first and second derivatives of the log-likelihood (2) with respect to a_i (at fixed λ) can be written as:

$$\frac{\partial L(y, \lambda, a)}{\partial a_i} = \sum_t p_{it} \frac{y_{it}}{\bar{y}_{it}} - p_i \tag{6}$$

$$\frac{\partial^2 L(y, \lambda, a)}{\partial a_i^2} = \sum_t -p_{it}^2 \frac{y_{it}}{\bar{y}_{it}^2} \leq 0 \tag{7}$$

If we consider only LORs i for which $y_{it} > 0$ and $p_{it} > 0$ for at least one TOF index t (an LOR with activity), the second derivative is strictly negative and the unconstrained maximizer

$$\tilde{a} = \arg\max_a L(y, \lambda, a) \tag{8}$$

is unique. This maximizer is a solution to $\partial L(y, \lambda, a)/\partial a_i = 0$ and satisfies

$$1 = \sum_t \frac{p_{it}}{p_i} \frac{y_{it}}{\tilde{a}_i p_{it} + s_{it}} \tag{9}$$

However, the attenuation factors are constrained and limited to $a_i \geq 0$. We show that (3) converges to the constrained maximizer (5), which has the following property:

$$a_i^* = \begin{cases} \tilde{a}_i, & \tilde{a}_i \geq 0 \\ 0, & \tilde{a}_i < 0 \end{cases} \tag{10}$$

To prove this, we analyze each case separately.

1) $\tilde{a}_i > 0$: It follows immediately from (9) that in this case, a fixed point of (3) is also the constrained maximizer a^* of the log-likelihood (2), provided that the fixed point is strictly positive. Furthermore,

- If $a_i^k < a_i^*$, then $a_i^k < a_i^{k+1} < a_i^*$.
  proof: When $a_i^k < a_i^*$, then $\partial L/\partial a_i|_{a^k} > 0$, because L is a concave function with a unique maximum. Inserting this in (3) one finds $a_i^k < a_i^{k+1}$. Furthermore, replacing a_i^k with a_i^* in (3) results in a larger increase of the numerator compared to the denominator (since $s_{it} \geq 0$, see section II-C for the case where $s_i = 0$), and therefore $a_i^{k+1} < a_i^*$.
- If $a_i^k > a_i^*$, then $a_i^k > a_i^{k+1} > a_i^*$.
  The proof is similar to the previous case except that in this case; $\partial L/\partial a_i|_{a^k} < 0$. Therefore, together with the previous case we see that starting from any strictly positive initial attenuation factor value $a_i^0 > 0$ the log-likelihood is not decreasing.
- The algorithm asymptotically converges to the fixed point a_i^*, i.e. $\lim_{k\to\infty} a_i^k = a_i^*$.
  proof: When λ is fixed, L is a concave function in a with a unique maximum. Combining (3) and (9) one obtains,

$$a_i^{k+1} - a_i^* = (a_i^k - a_i^*) \sum_t \frac{s_{it}}{(a_i^k p_{it} + s_{it})} \frac{p_{it}}{p_i} \frac{y_{it}}{(a_i^* p_{it} + s_{it})} \tag{11}$$

Using the fact that all quantities are non-negative and that an upper limit α_i can be found for the fraction

$s_{it}/(a_i^k p_{it} + s_{it})$ for each of the cases mentioned above, we have

$$\begin{aligned} |a_i^{k+1} - a_i^*| \quad &\leq \quad |a_i^k - a_i^*| \alpha_i \sum_t \frac{p_{it}}{p_i} \frac{y_{it}}{(a_i^* p_{it} + s_{it})} \\ &= \quad |a_i^k - a_i^*| \alpha_i \ \leq \ |a_i^0 - a_i^*| \alpha_i^{k+1} \end{aligned} \quad (12)$$

with,

$$\alpha_i = \begin{cases} \max\limits_{t, p_{it} > 0} (\dfrac{s_{it}}{a_i^0 p_{it} + s_{it}}), & a_i^0 < a_i^* \\ \max\limits_{t, p_{it} > 0} (\dfrac{s_{it}}{a_i^* p_{it} + s_{it}}), & a_i^0 \geq a_i^* \end{cases} \qquad (13)$$

where the restriction over the t range is due to the fact that terms with $p_{it} = 0$ do not contribute to the sum. Using this restriction together with $a_i^0 > 0$ and $a_i^* = \tilde{a}_i > 0$, one finds that $\alpha_i < 1$, $(\alpha_i)^k \to 0$ and therefore $|a_i^k - a_i^*| \to 0$. From this proof we expect a fast geometric convergence rate of order (scatter and randoms fraction)^k.

2) $\tilde{a}_i = 0$: When started with $a_i^0 > 0$, the sequence a_i^k is bounded below by zero because (3) preserves non-negativity, and is non-increasing because the derivative of the log-likelihood is negative for $a_i^k \geq \tilde{a}_i$. Therefore, this sequence converges to some $a_i^\dagger \geq 0$. However, if $a_i^\dagger > 0$, then $a_i^k \geq a_i^\dagger$ for all k and the upper limit α_i on a_i^k in (13) can be replaced by

$$\alpha_i = \max_{t, p_{it} > 0} (\frac{s_{it}}{a_i^\dagger p_{it} + s_{it}}) < 1 \qquad (14)$$

and hence $a_i^k \to 0$, which is in contradiction with the assumption that $a_i^\dagger > 0$. Therefore, $a_i^\dagger = 0 = a_i^*$.

3) $\tilde{a}_i < 0$: Since at fixed λ, L is a concave function with a unique maximum, it follows that:

$$\left. \frac{\partial L(y, \lambda, a)}{\partial a_i} \right|_{a_i = 0} < 0 \Leftrightarrow \sum_t \frac{p_{it}}{p_i} \frac{y_{it}}{s_{it}} < 1 \qquad (15)$$

which defines an upper limit to (3) such that:

$$a_i^{k+1} \leq a_i^k \{ \sum_t \frac{p_{it}}{p_i} \frac{y_{it}}{s_{it}} \} \qquad (16)$$

The factor in the brackets is independent of k and is strictly smaller than 1, therefore $a_i^k \to 0$.

C. Special Case of Zero Scatter and Randoms

As suggested above, the first step of the algorithm, equation (3), converges in a single iteration when the additive contribution s_{it} vanishes. Setting $s_{it} = 0$ in (3) and (4) results in the standard MLEM algorithm, except that in every iteration $k+1$ the attenuation factors a_i^{k+1} are replaced with y_i/p_i^h. In this case, there is no need for separate storage of the attenuation factor sinogram and the two step MLACF algorithm reduces to a single step MLEM-like algorithm:

$$\lambda_j^{h+1} = \quad \frac{\lambda_j^h}{\sum_i \frac{y_i}{p_i^h} c_{ij}} \sum\nolimits_{it} c_{ijt} \frac{y_{it}}{\sum_\xi c_{i\xi t} \lambda_\xi^h} \qquad (17)$$

Furthermore, inserting the new attenuation update (3) in the log-likelihood (2), and keeping only the terms that depend on λ, one obtains the reduced log-likelihood function ($\tilde{L}$):

$$\tilde{L}(y, \lambda) = \sum_i \sum_t y_{it} \log p_{it}(\lambda) - y_i \log p_i(\lambda). \qquad (18)$$

Although we currently have no results for the general log-likelihood (2), it is shown that for the case of consistent data the reduced log-likelihood function (18) has no local maxima other than the global maximum [15], [22]. In [22], [23], an alternative derivation of the MLEM-like algorithm (17) from the reduced log-likelihood function (18) is given, and it is shown that the proposed algorithm monotonically increases the likelihood and is asymptotically regular, i.e. the difference between consecutive reconstruction updates converges to zero.

III. EXPERIMENT DESIGN

The simulation parameters were chosen according to the Siemens Biograph mCT scanner specifications [25]. The 2D and 3D TOF-PET emission data consist of 200 radial bins of 0.4 cm width, 168 projection angles over 180 deg, and 13 TOF-bins of 312 ps width with an effective TOF resolution of 580 ps. In the 2D thorax simulations, the phantom was discretized in an image of 600×600 pixels and each LOR is simulated as the average of three LORs to introduce a slight mismatch between the simulation and reconstruction projectors. The 3D simulation (and patient) TOF-PET data are organized as 5D sinograms [26], consisting of 200 radial bins, 168 azimuthal angles, 7 (9) co-polar angles with 81 (109) planes of 0.2 cm width, and 13 time bins.

To simulate a reasonable scatter (and randoms) contribution, the noiseless emission sinograms were smoothed in the radial, angular, axial and TOF directions with a Gaussian kernel of 12 cm, 0.43 rad, 12 cm and 9.4 cm FWHM, respectively. The 2D and 3D simulated scatter estimates are scaled to obtain a scatter-to-primary ratio of 50%, and are added to the emission sinograms prior to adding Poisson noise to the measurements. For scatter correction, the exact noise-free scatter profile was used.

The 2D measurements are reconstructed in a 200 × 200 pixel grid with a pixel width of 0.4 cm and the reconstructed 3D activity and attenuation images had a 200 × 200 × 81 (× 109) voxel grid with a voxel width of 0.4 cm and 0.2 cm in the transaxial and axial directions, respectively. The algorithm was initialized with a uniform activity image and an attenuation factors sinogram of all ones. Activity figures are shown in a white-to-black color map whereas a black-to-white color map is used to show the attenuation images as well as the attenuation factors.

A. 2D Simulation

2D TOF-PET data were generated from the thorax phantom shown in figure 1. Activity reconstructions of the TOF-PET emission data are then generated with MLACF and compared to reconstructions of MLAA and MLEM with known attenuation. In MLAA [14], the activity and attenuation images are updated in an interleaved manner by keeping one of the

Fig. 1. 2D activity (left) and attenuation images (center) of the thorax and the corresponding attenuation factors (right).

images from the pair fixed while updating the other, and the non-negativity constraint is enforced on the attenuation image μ.

1) Reconstructions: MLACF, MLAA and MLEM reconstructions were analyzed for noise-free, moderate-noise and high-noise TOF-PET emission data. The moderate-noise and high-noise emission data have on average 31.9 and 6.4 maximum counts in the TOF sinogram, corresponding to 105.7 and 21.1 counts in their non-TOF sinograms, respectively. In the joint estimation methods (MLACF, MLAA), we assumed that the total amount of activity was known and the activity reconstructions were scaled during reconstructions accordingly. This (rather unrealistic) assumption is used because the TOF-PET data determine the activity and attenuation factors only up to a multiplicative constant.

In order to get more insight into the convergence properties of MLACF compared to MLAA and MLEM, the log-likelihood of equation (2) as well as the mean square difference (MSD) between the reconstructions and a converged reconstruction was computed within the support of the thorax phantom for each iteration of the three algorithms. In this study, no ordered subsets acceleration was applied, i.e. all projection angles were used in every iteration. The reconstruction of the 1000^{th} iteration was considered as the converged reconstruction, and the two measures were computed as a function of the number of iterations.

2) Noise Analysis: To analyze the noise properties of MLACF and MLAA, activity reconstructions were made (after 3 iterations of 42 subsets) with varying amounts of noise in the TOF-PET data. The lowest amount of noise in this study corresponds to the moderate-noise case described in the previous section. Five additional data sets were created, making a series of six data sets in all, where each data set has one-half the total counts of the previous data set in the series (so that the final image set has 1/32nd of the counts of the first data set). We assume that the noise-free activity reconstructions of MLACF and MLAA are good estimates for their respective mean activity reconstructions over multiple noise realizations. After subtracting the mean reconstruction from the noisy reconstructions, standard deviation and a noise correlation coefficient measure are computed for each noise level. As reference we use MLEM activity reconstructions and compute the noise correlation coefficients as:

$$NCC = \frac{\sum_{j\in\Omega}(\mathcal{N}_j^n - \mathcal{N}_j^f)(\mathcal{R}_j^n - \mathcal{R}_j^f)}{\sqrt{\sum_{j\in\Omega}(\mathcal{N}_j^n - \mathcal{N}_j^f)^2 \sum_{j\in\Omega}(\mathcal{R}_j^n - \mathcal{R}_j^f)^2}} \qquad (19)$$

where, $\mathcal{N}$ is the MLACF or MLAA activity reconstruction, $\mathcal{R}$ defines the reference MLEM activity reconstruction, superscripts ^{n} and ^{f} correspond to noisy and noise-free reconstructions, respectively, j is the pixel index, and Ω determines the support of the activity image.

3) Bias-Variance: With the same level of noise as in the high-noise level case, we study bias and variance of the MLACF activity reconstructions and compare the results to bias and variance curves of MLAA and MLEM emission reconstructions as a function of activity reconstruction updates. All three algorithms are initialized with the same initial activity image, i.e. uniform disk of activity. Just as before, the reconstructions are scaled in each update according to the total amount of activity in the reconstructed activity image. Bias and variance estimates are then computed in the support of the 2D thorax phantom for 150 iterations of the three algorithms. In this study, no ordered subsets acceleration was applied. As before, we assume that a noise-free reconstruction of the thorax phantom is a good estimate of the average of noisy reconstructions from multiple noise realizations. In each iteration, bias is computed as the average absolute pixel-by-pixel difference between the noise-free reconstruction and the activity phantom of figure 1. It is reported with the variance of activity reconstructions of 100 different TOF-PET noise realizations.

When going from 2D to 3D TOF-PET, the number of unknown attenuation factors (i.e. the size of the sinogram) increases dramatically, due to the inclusion of all the oblique lines. To keep the simulations simple and fast, we model a similar effect by a three-fold increase in the number of angles of the 2D bias-variance study. By doing so, the total counts in the sinogram increases three-fold, however the expected count per pixel remains the same. We compare the results of MLACF to those of the standard MLEM and MLAA algorithms. We expect that this overdetermined 2D bias-variance analysis will be predictive of the noise properties in the fully 3D case. The bias and variance measures are again computed within the support of the 2D phantom for 150 iterations, and the measures are computed from a noise-free activity reconstruction as well as activity reconstructions from 50 different noise realizations of the TOF-PET emission data.

B. 3D Simulation

Figure 2 shows the activity and attenuation images of the NCAT phantom used in our 3D simulation study. The

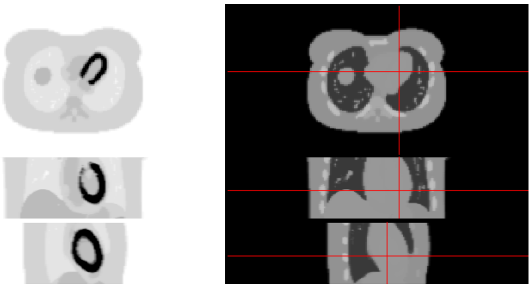

Fig. 2. Transaxial (top), coronal (middle) and sagittal (bottom) views of the NCAT activity (left) and attenuation (right) images used in the 3D study.

NCAT phantom was forward projected with a 3D TOF-PET projector, scatter (with a scatter-to-primary ratio of 50%) was added to the noise-free emission data and Poisson noise was added to the measurements. The resulting TOF sinogram had a maximum count of 24, while its corresponding non-TOF sinogram had a maximum count of 56. The MLACF activity reconstruction was then compared to MLAA and MLEM activity reconstructions. As before, we assumed that the total amount of activity was known, hence the joint reconstructions were scaled accordingly.

C. *Patient data*

A clinical 4 minute TOF-PET thorax scan of a patient injected with 296 MBq of ^{18}F-FDG is reconstructed with MLACF and compared to activity reconstructions of MLAA and MLEM. The emission data is acquired 80 minutes post-injection, and the scatter and randoms fraction of the TOF emission data are 19% and 45%, respectively.

D. *Self-Normalizing Algorithm*

2D detector sensitivities were simulated mimicking transaxial detector pair sensitivities of the Biograph mCT scanner. The sensitivity variations are dominated by the gaps between the detector blocks with streak artifacts similar to the ones produced by faulty detector blocks [26]. However, in addition to the latter effect, detector pair variabilities were also accounted for by assigning a random value generated from a uniform distribution in $(0.95, 1.05)$ to LORs which were not affected by the "gap effect". 2D TOF-PET measurements of the thorax phantom (figure 1) were simulated, taking into account these detector sensitivities. Activity images were then reconstructed with MLACF using two approaches. In the first one, the simulated detector pair sensitivities are taken into account by modeling them into the system matrix c_{ijt}. In the second approach, the sensitivities are ignored altogether, hence MLACF needs to estimate the product of the attenuation factors and the sensitivities. Activity reconstructions were also made ignoring the Biograph mCT scanner sensitivities for the 4 minute patient data.

IV. Results

A. *2D Simulation*

1) Reconstructions: MLACF, MLAA and MLEM activity reconstructions from the noise-free data are shown in figure 3. The figure also shows the MLACF attenuation image computed by post-reconstruction of the attenuation factors, together with MLAA estimated attenuation factors obtained by projection of the attenuation reconstruction (they have been computed to enable comparison of the MLAA and MLACF results). MLACF reconstructions are after 3 iterations of 42 subsets where the attenuation factor estimate (equation (3)) is updated 3 times for each update of the activity (equation (4)). The MLACF attenuation image was reconstructed with 5 iterations of 42 subsets of the MLEM algorithm from the logarithm of the estimated attenuation factors assuming there was no attenuation along LORs without activity. The MLAA reconstructions are after 3 iterations of 42 subsets where the attenuation reconstruction is updated 3 times for each update of the activity [14]. MLEM reconstructions are after the same number of activity updates as MLACF and MLAA (3 iterations of 42 subsets). It should be mentioned that the ratio of three updates of the attenuation (sinogram in MLACF or image in MLAA) to one update of the activity image is empirical and was not rigorously optimized.

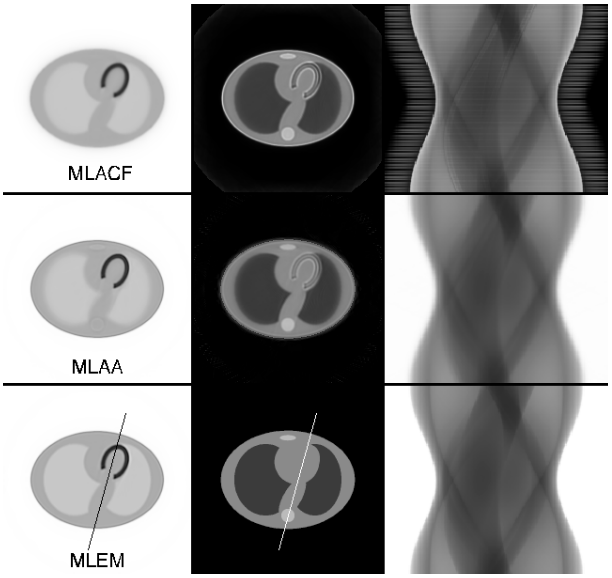

Fig. 3. MLACF (top), MLAA (middle) and MLEM (bottom) reconstructions of the activity image (left), attenuation image (center) and attenuation factors (right) of the noise-free TOF-PET emission data. The true attenuation image and sinogram are shown for comparison in the third row.

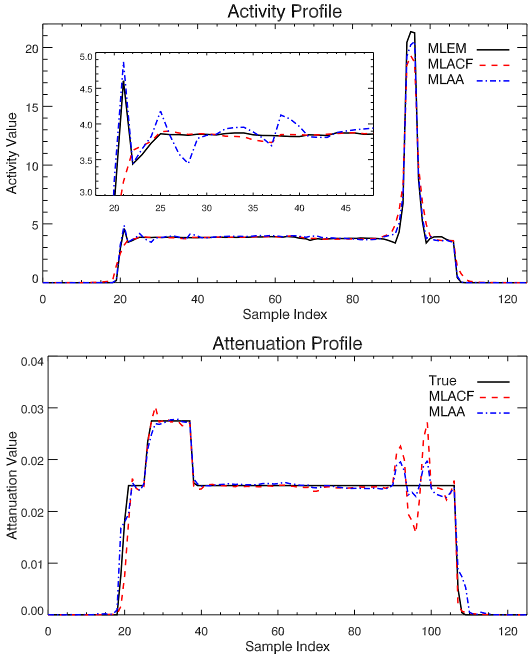

Fig. 4. Activity (top) and attenuation (bottom) profiles through MLACF and MLAA reconstructions of noise-free data plotted against reference MLEM activity and the true attenuation profiles, respectively. The profiles correspond to the lines depicted in figure 3.

Figure 4 shows profiles through the reconstructed MLACF, MLAA and MLEM activity images together with the attenuation profiles of MLACF and MLAA attenuation reconstructions and the true attenuation images. The activity profile shows that MLACF suffers less from artifacts in regions with strong attenuation gradients than MLAA. However, the post-reconstructed attenuation profile of MLACF seems to be more sensitive in regions with a strong change of activity.

Figure 5 shows MLACF and MLAA reconstructions when the emission data are corrupted by Poisson noise. The displayed activity reconstructions of the high-noise case are scaled and shown in the same color map as the moderate-noise case. It is interesting to see that the attenuation factors of MLACF tend to be noisier than the attenuation estimates of MLAA. This is due to the fundamental difference between the two algorithms and is the result of the consistency of the attenuation factors in MLAA.

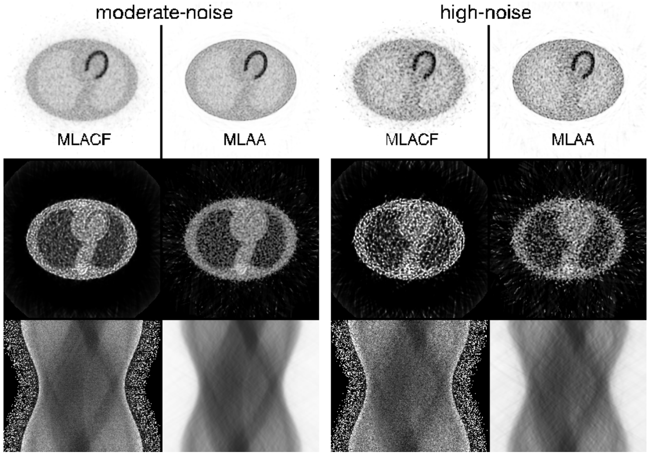

Fig. 5. MLACF (columns 1,3) and MLAA (columns 2,4) reconstructions of the activity image (top), attenuation image (middle) and attenuation factors (bottom). The reconstructions are for moderate (columns 1,2) and high (column 3,4) Poisson noise in the TOF-PET emission data. The high-noise activity reconstructions are scaled to be shown in the same color map as moderate-noise activity reconstructions.

Figure 6 shows the log-likelihood (2) normalized to the upper-limit of (2) determined by the data, i.e. $\sum_{it} y_{it} \ln y_{it} - y_{it}$, as well as the MSD of the reconstructions normalized to have the same total amount of activity as the activity phantom for the noise-free and the high-noise TOF-PET emission simulations. It is interesting to see that for the joint estimation methods, the log-likelihood and MSD rank the convergence of the algorithms differently. We believe that convergence as measured by the MSD better reflects the clinically relevant behaviour of the algorithms. Figure 6 shows that the MLACF reconstructions are slower to converge compared to the MLAA and MLEM reconstructions. However it should be mentioned that while MLAA has a faster convergence rate, it is also computationally more demanding. It is also worth noting that because MLACF does not require consistency of the attenuation factors, it has more degrees of freedom to explain the TOF-PET emission data. Hence, it produces a higher likelihood in the case of noisy data, with the difference to reference MLAA and MLEM computed likelihoods increasing with increasing amount of noise in the TOF-PET emission data.

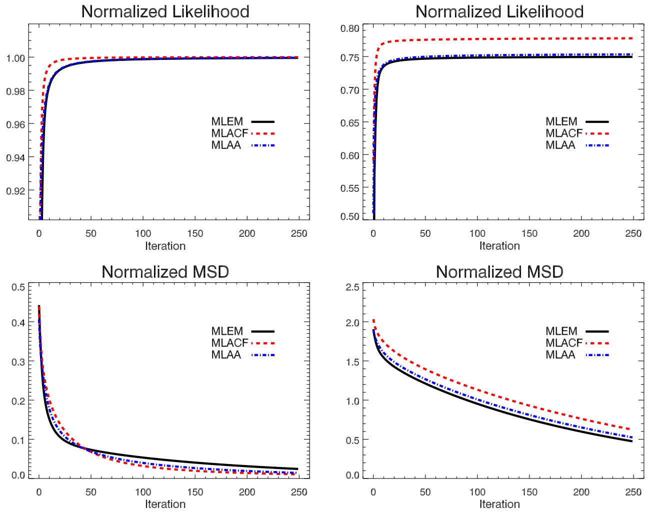

Fig. 6. Log-likelihood of equation (2) (top) and the MSD measure (bottom) for MLACF, MLAA and MLEM reconstructions of the noise-free (left) and high-noise (right) TOF-PET emission data.

2) *Noise Analysis :* Figure 7 shows the standard deviation of the two algorithms, which are comparable except for extreme-noise in the emission data. Figure 7 also shows the computed noise correlation coefficients of MLACF and MLAA with varying amounts of noise in the data. The noise of the MLAA activity reconstructions is highly correlated to the noise in the MLEM images in all cases. In contrast, the MLACF noise is less correlated to the MLEM noise, and the correlation decreases for increasing amounts of noise in the TOF-PET emission data.

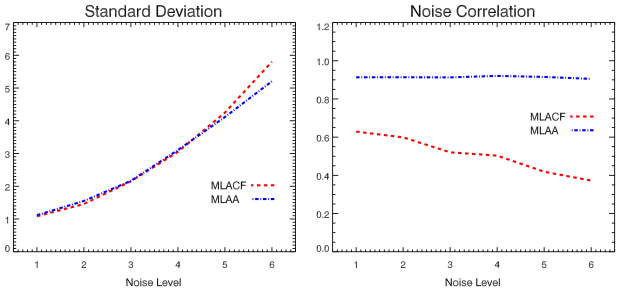

Fig. 7. Standard deviation (left) of MLACF and MLAA activity reconstructions, and their noise correlation coefficient (right) with reference MLEM activity reconstructions computed using (19) for varying noise levels in the TOF-PET emission data.

3) *Bias-Variance:* The bias-variance curves of the 2D activity reconstructions of MLACF, MLAA and MLEM can be seen in figure 8, where bias and variance are computed for each update of the activity reconstructions. The reconstructions are for a high level of noise in the TOF-PET emission data (corresponding to a maximum count of 6.4 in the TOF sinogram). The curves are computed for a total of 150 updates of the activity reconstructions with all the projections used to update the reconstructions (no ordered subsets acceleration). Although in early iterations MLAA is able to achieve lower bias for the same level of variance than

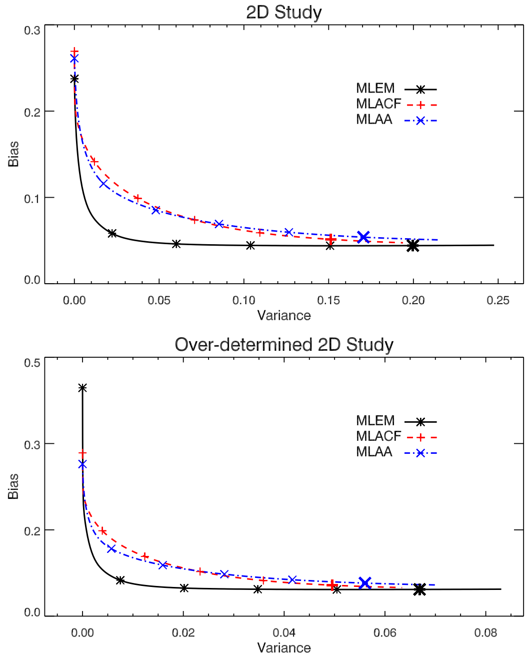

Fig. 8. 2D (top) and overdetermined 2D (bottom) bias-variance curves for MLACF, MLAA and MLEM activity reconstructions from 100 and 50 noise realizations, respectively. The marked points on the curves are bias and variance values after 25 updates of the three algorithms. The bold symbols are bias and variance values for 126 (corresponding to 3 iterations of 42 subsets) reconstruction updates.

MLACF, the MLACF reconstructions have lower bias closer to convergence. However, the difference between the two curves is small.

Figure 8 also shows the bias-variance curves of the overdetermined 2D activity reconstructions of MLACF, MLAA and MLEM. With the increased total sinogram count, the three algorithms produced images with decreased variance. As before, MLACF and MLAA had similar performance and were outperformed by MLEM, in particular at lower iterations. This suggests that the 3D activity reconstructions of MLACF will have similar bias and noise properties as activity reconstructions of MLAA.

B. 3D Simulation

Figure 9 shows MLACF, MLAA and MLEM activity reconstructions of the 3D NCAT phantom. The figure also shows the estimated MLACF, estimated (and projected) MLAA and the true attenuation factors of the transaxial slice of the NCAT phantom. The activity reconstructions of the three algorithms were generated after 3 iterations of 42 subsets, and displayed after post-smoothing the activity distributions with a Gaussian of 0.6 cm FWHM. The activity reconstructions of the three algorithms are comparable. However, the MLACF reconstruction is more noisy outside the support of the NCAT phantom. This is because only LORs that intersect the phantom support contain information about the attenuation factors. Because segmenting these LORs is not straightforward, we have not attempted to identify these LORs to impose an attenuation factor of 1. Consequently, these LORs are assigned arbitrary values, and because of this non-zero background attenuation, the reconstructed activity outside the object is increased as well.

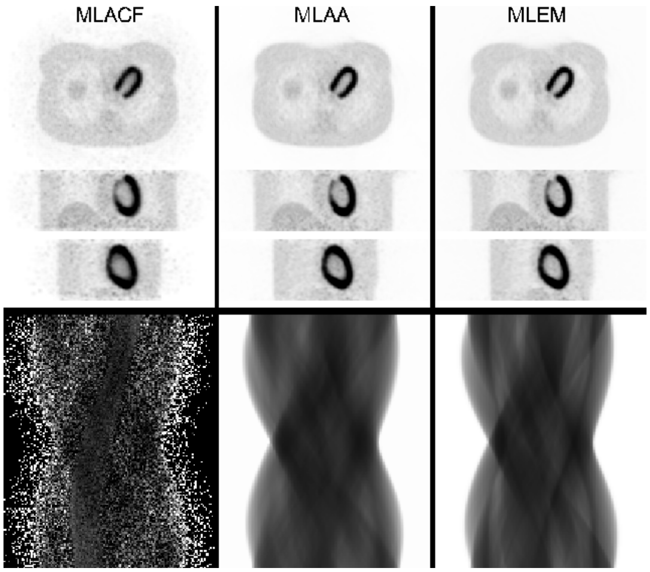

Fig. 9. MLACF (left), MLAA (center) and MLEM (right) activity reconstructions (top) of the NCAT phantom post-smoothed with a Gaussian of 0.6 cm FWHM, together with the estimated MLACF, estimated MLAA and the true attenuation factors (bottom) for the transaxial slice of the 3D NCAT phantom.

C. Patient data

Figure 10 shows MLACF, MLAA and MLEM activity reconstructions of the 4 minute ^{18}F-FDG patient data. The MLACF and MLAA reconstructions are scaled in each iteration to have the same amount of tracer activity as the MLEM reconstruction. The displayed activity reconstructions are smoothed with a Gaussian of 0.6 cm FWHM. Just as in the 3D simulation, the activity reconstructions are comparable, except for increased activity values outside the support of the patient. However, close inspection reveals that activity reconstructions of MLAA and MLACF suffer less from shadow-like artifacts [3] near the dome of the liver and the lateral wall of the heart (arrows in red) than the activity reconstruction of MLEM. This is indication to a geometric mismatch between PET emission data and CT-attenuation factors, which is expected since the CT was obtained in a breath-hold position.

D. Self-Normalizing Algorithm

Figure 11 shows MLACF activity reconstructions of the 2D thorax phantom together with the estimated attenuation factors, with and without correction for detector pair sensitivities during reconstructions. Figure 12 shows MLACF activity reconstructions of the patient data with and without correction for detector pair sensitivities during reconstructions. For comparison MLEM reconstructions of the patient data are also shown when detector pair sensitivities are not taken into account. The activity images displayed are after smoothing the reconstructions with a Gaussian of 0.6 cm FWHM. Figure 13 shows the estimated attenuation factors of MLACF when detector pair sensitivities are ignored. For comparison the

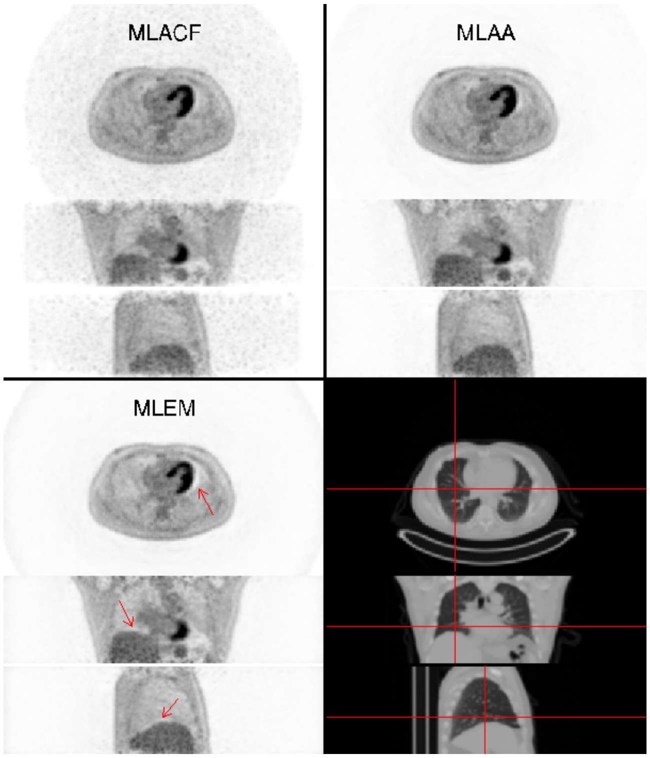

Fig. 10. Transaxial, coronal and sagittal views of MLACF (top-left), MLAA (top-right) and MLEM (bottom-left) activity reconstructions of the 4 minute ^{18}F-FDG patient data post-smoothed with a Gaussian of 0.6 cm FWHM. The MLEM activity reconstruction was obtained taking into account the CT-based attenuation image (bottom-right). The arrows indicate artifacts due to respiratory motion, which are more severe in the MLEM reconstructions.

product of the CT-attenuation factors and detector sensitivities is also shown.

V. DISCUSSION

Joint reconstruction of activity and attenuation has gained a lot of interest since it was shown and proven that TOF-PET data provide information about attenuation that was not previously available. In the same spirit, this paper proposes a maximum likelihood approach to jointly estimate the activity image together with the attenuation factors. Because the TOF-PET data determine the solution only up to a scale, some prior knowledge is required to obtain accurate quantification. Because MLAA estimates the attenuation image, it is straightforward to impose the known tissue attenuation value. Since MLACF does not estimate the attenuation image, one may have to find ways to obtain prior knowledge about the tracer distribution. In this study, we have simply assumed that the total amount of activity in the field of view was known. In practice, it may be difficult to obtain this kind of knowledge, unless one accepts to add objects with a known activity in the field of view. However, in some cases, it may be possible to obtain (partial) information about the attenuation factors to solve the scale problem. E.g., it may be possible to use the noisy transmission data provided by the Lu background radiation in LSO and LYSO scanners [27]. In [28], a modified version of the algorithm was proposed that made use of the partially known CT-attenuation factors.

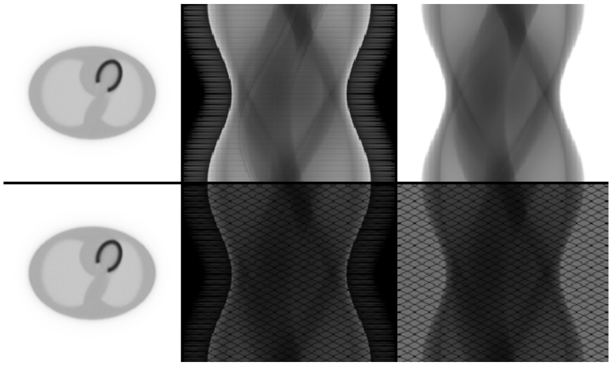

Fig. 11. MLACF reconstructions of the activity image (left) and attenuation factors (center) when the detector pair sensitivities are taken into account (top) and when they are ignored (bottom). The true attenuation factors (top-right) and their multiplication with detector pair sensitivities (bottom-right) are shown for comparison.

In contrast to MLAA, this algorithm does not enforce consistency of the attenuation factors. As a consequence, MLACF activity reconstructions were expected to be noisier than their MLEM and MLAA counterparts. Although the noise structure in the activity reconstructions of MLACF and MLAA seems to be different, the noise realization study showed little difference between their bias-variance curves. However, under extremely noisy conditions MLACF activity reconstructions seem to be influenced more by noise than MLAA reconstructions (figure 7, left panel). Compared to MLAA, MLACF requires fewer (back-) projections in every iteration of the algorithm. In the 3D simulations, the computation time of an MLAA iteration

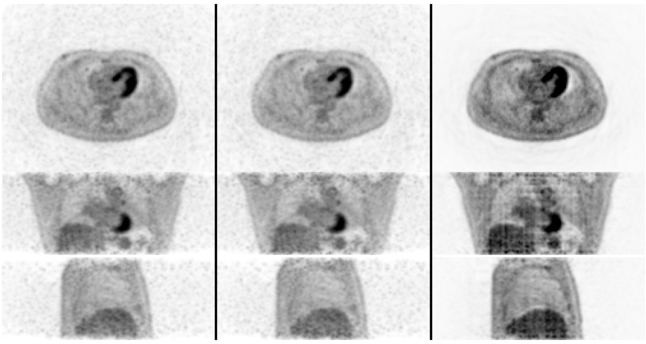

Fig. 12. MLACF reconstructions of the tracer activity when the detector pair sensitivities are taken into account (same MLACF reconstruction as figure 10) (left). MLACF (center) and MLEM (right) activity reconstructions when detector pair sensitivities are ignored during reconstruction. The reconstructions are post-smoothed with a Gaussian of 0.6 cm FWHM.

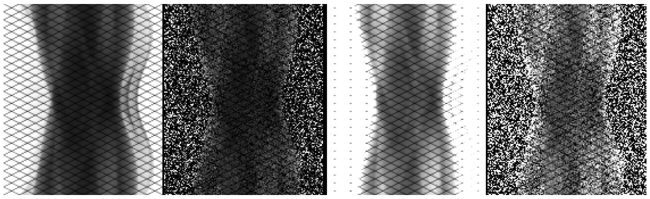

Fig. 13. CT-attenuation factors multiplied by detector pair sensitivities shown together with the MLACF estimated attenuation factors ignoring detector pair sensitivities (left pair) for the transaxial slice of figure 12. The same attenuation factors are shown with a different gray level scale (right pair).

was roughly 2.5 times longer than that of an MLACF iteration.

Furthermore, the two joint estimation algorithms seem to respond differently to gradients in the attenuation image, where MLACF seems to have an advantage over MLAA (figure 4). A similar response was also observed in regions of the activity image with a high activity gradient, e.g. near the heart of the 2D thorax phantom (see the activity and attenuation profiles around sample index 90 in Figure 4). In the MLAA (and MLEM) reconstruction Gibbs over- and undershoots were observed in earlier iterations compared to MLACF reconstructions. We believe that in MLACF these high frequency elements are initially incorporated in the attenuation factors, where they cause the artifacts seen when this sinogram is reconstructed. Our current tests indicate that in the absence of noise the differences between the images of two algorithms tend to reduce at high iteration numbers, and the activity reconstructions become comparable. This suggests that they are mostly caused by different trajectories towards the solution, and much less by differences in the final solutions. The study of these effects are subject to future investigations.

Convergence of the attenuation estimate of MLACF (update expression (3)) is shown to be geometric with a ratio equal to the scatter fraction of the emission data. If the scatter and randoms contribution in the measurements can be ignored, the algorithm reduces to an MLEM-like algorithm with an immediate convergence of the attenuation factors. Properties and some convergence results for such an algorithm can be found in [15], [22], [23], where it is also proven that the log-likelihood is free of local maxima for consistent TOF emission measurements.

In the clinical system considered here, the scatter contribution is estimated from the CT-based attenuation coefficients [29]. We have used this scatter estimate in the MLACF reconstruction of the patient data. However, we believe that, if required, a scatter estimate independent of the CT could be obtained as well, from a first MLACF reconstruction where the scatter is ignored. From the estimated attenuation sinogram, an approximate attenuation map could be reconstructed, which could be used to estimate the scatter. With this estimate, MLACF could be applied again to obtain scatter corrected activity estimates. In [14], some evidence was given that this procedure would work for MLAA, which makes us believe that it could be applied to MLACF as well.

The proposed method proves to be very robust against variations in detector pair sensitivities. This was demonstrated with reconstructions where detector pair sensitivities were ignored for a 4 minute ^{18}F-FDG scan of a patient thorax. Although MLACF obtained almost identical activity images when detector pair sensitivities were ignored or accounted for, we do not propose to ignore the sensitivities during reconstructions. When the sensitivities are estimated by means of dedicated high count calibration scans, the detector pair sensitivities are estimated with greater precision. Moreover, using the estimated sensitivities during MLACF reconstructions allows the reconstruction of the attenuation image if needed, which otherwise is not possible. But the results show that MLACF will automatically compensate for any residual calibration errors that might be present in the estimated sensitivities.

In the patient study, we observed shadow-like artifacts in MLEM reconstructions of the activity which were not present in the activity estimates of MLACF and MLAA. We believe that these artifacts are caused by motion between the CT and PET scans, and that these artifacts can be mitigated by algorithms which jointly estimate the activity and the attenuation.

VI. CONCLUSION

This paper introduces a new algorithm in the framework of joint activity and attenuation reconstructions from TOF-PET data. The MLACF algorithm, which makes alternating updates of the activity and the attenuation factors, worked well in our 2D and 3D simulations as well as in a patient scan. Although MLACF does not impose consistency to the estimated attenuation factors, the activity reconstructions possess similar noise characteristics as activity reconstructions of MLAA for considerable amounts of noise in the emission data. The method also proves to be a powerful tool in case of inaccurate estimates of detector pair sensitivities which otherwise can cause image degradation in the reconstructions.

VII. ACKNOWLEDGEMENT

The authors would like to thank A. Bousse for his comments which helped improve the convergence analysis, and C. Michel, M. Casey, G. Bal, F. Kehren, M. Conti, C. Watson, V. Panin and J. Hamill from Siemens Healthcare, Molecular Imaging for help with the data processing and the very interesting discussions. The authors would also like to thank S. Stroobants, S. Staelens and M. Lambrechts of the Universiteit Antwerpen for providing the patient data.

REFERENCES

[1] PE Kinahan, DW Townsend, T Beyer *et al.*, “Attenuation correction for a combined 3D PET/CT scanner”, *Med Phys*, 1998, 25(10):2046-2053.

[2] H Zaidi, BH Hasegawa, “Attenuation correction strategies in Emission Tomography”, in *Qualitative analysis in nuclear medicine imaging*, H Zaidi, Springer Science + Business Media Inc. 2006

[3] MM Osman, C Cohade, Y Nakamoto, RL Wahl, “Respiratory motion artifact on PET emission images obtained using CT attenuation correction on PET-CT”, *Eur J Nucl Med Mol Imaging* 2003, 30(4):603-606.

[4] Y Censor, DE Gustafson, A Lent, H Tuy, “A new approach to the emission computerized tomography problem: simultaneous calculation of attenuation and activity coefficients”, *IEEE Trans Nucl Sci*, 1979, 26(2):2775-2279.

[5] F Natterer, “Determination of tissue attenuation in emission tomography of optically dense media”, *Inverse Problems*, 1993, 9(6):731-736.

[6] A Welch, R Clack, F Natterer *et al.*, “Toward accurate attenuation correction in SPECT without transmission measurements”, *IEEE Trans Med Imaging*, 1997, 16(5):532-541.

[7] J Nuyts, P Dupont, S Stroobants *et al.*, “Simultaneous maximum a-posteriori reconstruction of attenuation and activity distributions from emission sinograms”, *IEEE Trans Med Imaging*, 1999, 18(5):393-403.

[8] AV Bronnikov, “Reconstruction of attenuation map using discrete consistency conditions”, *IEEE Trans Med Imaging*, 2000, 19(5):451-462.

[9] H Kudo, H Nakamura, “A new approach to SPECT attenuation correction without transmission measurements”, *IEEE Nucl Sci Symp Conf Record*, Oct-2000, 2(13):58-62.

[10] VY Panin, GL Zeng, GT Gullberg, “A method of attenuation map and emission activity reconstruction from emission data”, *IEEE Trans Nuc. Science*, 2001, 48(1):131-138.

[11] A Krol, JE Bowsher, SH Manglos *et al.*, “An EM algorithm for estimating SPECT emission and transmission parameters from emission data only”, *IEEE Trans Med Imaging*, 2001, 20(3):218-232.

[12] F Crepaldi, A De Pierro, "Activity and attenuation recovery from activity data only in emission computed tomography", *IEEE Trans Nuc. Science*, 2007, 54:100-106.

[13] A Salomon, A Goedicke, B Schweizer *et al.*, "Simultaneous reconstruction of activity and attenuation for PET/MR", *IEEE Trans Med Imaging*, 2011, 30(3):804-813.

[14] A Rezaei, M Defrise, G Bal, C Michel, M Conti, C Watson, J Nuyts, "Simultaneous reconstruction of activity and attenuation in Time-of-flight PET", *IEEE Trans. Med. Imag.*, 2012, 31(12):2224-2233.

[15] J Nuyts, A Rezaei, M Defrise, "ML-reconstruction for TOF-PET with simultaneous estimation of the attenuation factors", *2012 IEEE Nuclear Science Symposium and Medical Imaging Conference, Anaheim*, 2012, pp. 2147-2149.

[16] M Defrise, A Rezaei, J Nuyts, "Time-of-flight PET data determine the attenuation sinogram up to a constant", *Phys Med Biol*, 2012, 57(4):885-899.

[17] M Defrise, DW Townsend, D Bailey, A Geissbuhler, T Jones, "A normalization technique for 3-D PET data", *Phys Med Biol*, 1991, 36(7):939-952.

[18] PE Kinahan, DW Townsend, DL Bailey, D Sashin, F Jadali, MA Mintun, "Efficiency normalization techniques for 3-D PET data", *1995 IEEE Nuclear Science Symposium and Medical Imaging Conference, Anaheim*, 1995, pp. 1021-1025.

[19] ML Camborde, A Rhamim, DF Newport, S Siegel, KR Buckley, E Vandevoort, TJ Ruth, V Sossi, "Effect of normalization method on image uniformity and binding potential estimates on microPET", *2004 IEEE Nuclear Science Symposium and Medical Imaging Conference, Anaheim*, 2004, pp. 3467-3471.

[20] RD Badawi, P Marsden, "Self-normalization of emission data in 3-D PET" *IEEE Trans Nucl Med*, 1999, 46(3), 706-712.

[21] A Salomon, B Goldschmidt, R Botnar, F Kiessling, V Schulz, "A Self-Normalization Reconstruction Technique for PET Scans Using the Positron Emission Data", *IEEE Trans. Med. Imag.*, 2012, 31(12):2234-2240.

[22] M Defrise, A Rezaei, J Nuyts, "Transmission-less attenuation correction in time-of-flight PET: analysis of a discrete iterative algorithm", *Phys Med Biol*, 2014, 59:1073-1095.

[23] M Defrise, A Rezaei, J Nuyts, "Simultaneous reconstruction of attenuation and activity in TOF-PET: analysis of the convergence of the MLACF algorithm", *Fully 3D meeting*, June 2013.

[24] AR De Pierro, "A Modified Expectation Maximization Algorithm for Penalized Likelihood Estimation in Emission Tomography", *IEEE Trans. Med. Imag.*, 1995, 14(1):132-137.

[25] BW Jakoby, Y Bercier, M Conti *et al.*, "Physical and clinical performance of the mCT time-of-flight PET/CT scanner", *Phys Med Biol* 2011, 56(8):2375-2389.

[26] FH Fahey, "Data acquisition in PET imaging", *J Nucl. Med. Technol*, 2002, 30(2):39-49.

[27] H Rothfuss, V Panin, I Hong, A Moor, J Young, J Hamill, C Michel, M Casey, "LSO Background Radiation as a Transmission Source Using Time of Flight Information", *2012 IEEE Nuclear Science Symposium and Medical Imaging Conference, Seoul*, 2013, paper M02-2.

[28] VY Panin, M Defrise, J Nuyts, A Rezaei, ME Casey, "Reconstruction of Uniform Sensitivity Emission Image with Partially Known Axial Attenuation Information in PET-CT Scanners" *2012 IEEE Nuclear Science Symposium and Medical Imaging Conference, Anaheim*, 2012, pp. 2166-2173.

[29] CC Watson, "Extension of single scatter simulation to scatter correction of time-of-flight PET", *IEEE Trans Nuc. Science*, 2007, 54(5):1679-1686.